BNL-225048-2023-JAAM

Multi-element metasurface system for imaging in the near-infrared

S. Shrestha, M. Lu

To be published in "Applied Physics Letters"

May 2023

Center for Functional Nanomaterials

Brookhaven National Laboratory

U.S. Department of Energy

USDOE Office of Science (SC), Basic Energy Sciences (BES) (SC-22)

Notice: This manuscript has been authored by employees of Brookhaven Science Associates, LLC under Contract No.DE-SC0012704 with the U.S. Department of Energy. The publisher by accepting the manuscript for publication acknowledges that the United States Government retains a non-exclusive, paid-up, irrevocable, world-wide license to publish or reproduce the published form of this manuscript, or allow others to do so, for United States Government purposes.

DISCLAIMER

This report was prepared as an account of work sponsored by an agency of the United States Government. Neither the United States Government nor any agency thereof, nor any of their employees, nor any of their contractors, subcontractors, or their employees, makes any warranty, express or implied, or assumes any legal liability or responsibility for the accuracy, completeness, or any third party's use or the results of such use of any information, apparatus, product, or process disclosed, or represents that its use would not infringe privately owned rights. Reference herein to any specific commercial product, process, or service by trade name, trademark, manufacturer, or otherwise, does not necessarily constitute or imply its endorsement, recommendation, or favoring by the United States Government or any agency thereof or its contractors or subcontractors. The views and opinions of authors expressed herein do not necessarily state or reflect those of the United States Government or any agency thereof.

Multi-element metasurface system for imaging in the near-infrared

Sajan Shrestha[1], Adam Overvig[1,2], Ming Lu[3], Aaron Stein[3], and Nanfang Yu[1,*]

[1]Department of Applied Physics and Applied Mathematics, Columbia University, New York, NY, 10027, USA
[2]Photonics Initiative, Advanced Science Research Center at the Graduate Center of the City University of New York, New York, NY, 10031, USA
[3]Brookhaven National Laboratory, Center for Functional Nanomaterials, Upton, NY 11973, USA
*Corresponding author: ny2214@columbia.edu

Abstract

Metasurfaces are optically thin 2D arrays of subwavelength scatterers that modify scalar and vector properties of incident electromagnetic fields. Metasurface lenses are of particular interest for imaging applications for their flat form factor, compatibility with CMOS fabrication processes, and potential for correcting aberrations with a small number of elements. We advance this capability by realizing a millimeter-diameter, polarization-independent metalens triplet system with chromatic aberration correction over the wavelength range of 1.30 to 1.60 μm, and monochromatic aberration correction enabling a field of view of 50°.

Advances in compact imaging [1]-[2], LiDAR [3]-[4], augmented/virtual reality [5]-[7], and medical imaging [8] devices have fueled interest and attention in high-performance, light-weight, and compact optical systems using flat optics. Conventionally, these systems require multiple refractive optical elements stacked together to correct optical aberrations [9]. In high-performance systems, manufacturing of the elements requires meticulous grinding and polishing of different types of glasses, followed by precise alignment of individual elements. Planar optical metasurfaces [10]-[16] are promising candidates to replace refractive optical elements in these systems due to their flat formfactor, which may facilitate integration in compact optical systems. Furthermore, optical metasurfaces can be fabricated using conventional thin-film growth, lithographic, and etching techniques employed in CMOS foundries, suggesting the possibility of high-throughput and high-yield manufacturing of flat optical components, and the possibility of integrating such components directly on top of imaging sensors.

Metasurfaces can realize many optical functionalities [17]-[22] by encoding suitable phase, amplitude, and/or polarization responses to individual subwavelength elements called meta-atoms. Using meta-atoms of high-index dielectric materials, highly efficient [23]-[27] metasurfaces have been recently demonstrated for various applications [28]-[32]. Singlet metalenses implementing an analytical phase function are well-known to produce diffraction-limited focal spots free of spherical aberration for normally incident light. However, away from the design wavelength, significant chromatic aberrations will be present, and for light at oblique incident angles, significant monochromatic aberrations will degrade imaging performance.

While chromatic aberrations have been corrected in refractive optical system by using multiple lenses [33] with different material dispersion or by adding diffractive components [34],[35], achromatic focusing across a continuous wavelength range in metalenses can be achieved by controlling the dispersive response [36] of individual meta-atoms. Achromatic metalens singlets working in the visible [37],[38] and the near-infrared [39] have been reported in recent works. Our previous work [39] has demonstrated polarization-insensitive achromatic focusing in the near-infrared across a wavelength range of 1200 – 1600 nm by using structural dispersion engineered meta-atoms.

Enlarging the field of view (FOV) via correction of monochromatic aberrations such as coma and astigmatism is equally important for imaging systems, but cannot be easily achieved by a single metalens due to the fact that individual meta-atoms, being optically small, primarily produce spherical scattered wavefronts (Huygens' wavelets), which are invariant as a function of angle. However, compound metasurface systems [40]-[42] can be optimized to correct monochromatic aberrations. In particular, metalens doublets operating in the near-infrared [1] and visible [2] have been reported recently with a FOV of up to 60˚. However, these demonstrations lack chromatic aberration corrections and so are not generally suitable for broadband imaging. Many other multi-element designs have been reported to extend the control of optical wavefront across multiple wavelengths [43]-[47] or incident angles [48], and recently, numerical studies using doublets [49],[50] or an aperture stop [51] have demonstrated combined aberration correction. However, none have been reported to correct both chromatic and monochromatic aberrations experimentally over a large FOV and continuous bandwidth. In this report, we demonstrate a polarization-insensitive metalens triplet designed to correct both chromatic and monochromatic aberrations across a continuous wavelength range in the near-infrared and with a FOV of 50˚.

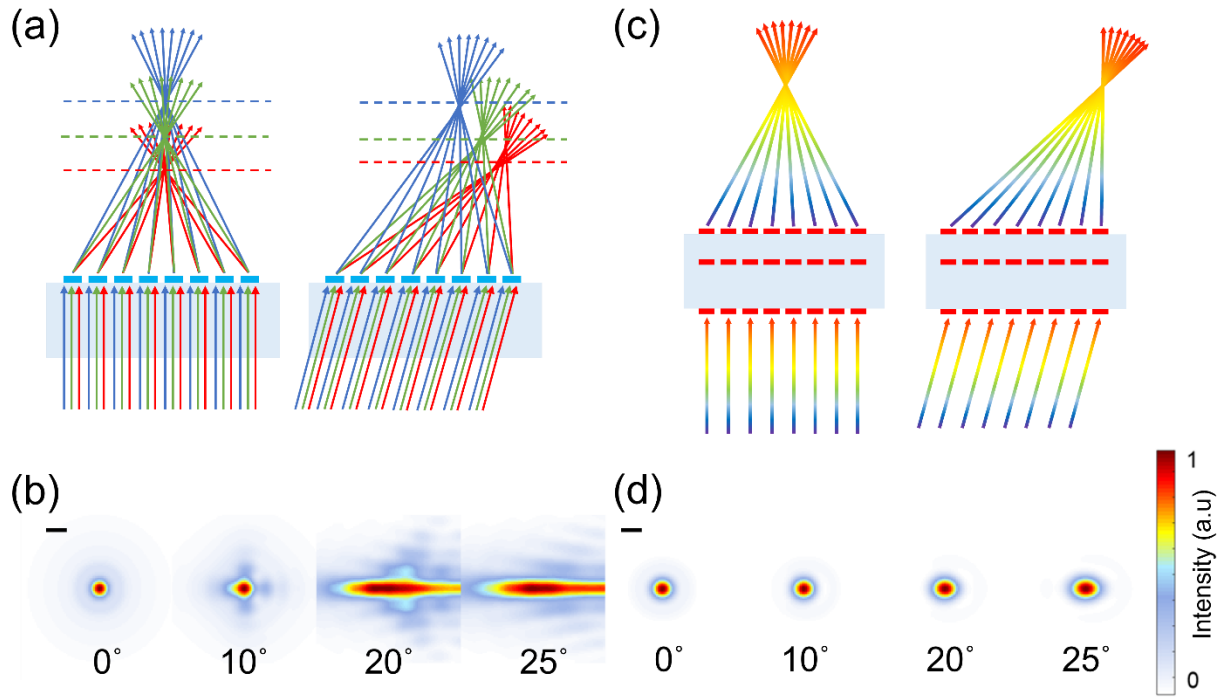

Fig. 1. Correcting optical aberrations. (a,c) Illustrations of ray focusing by a metalens singlet (a) and triplet (c) for light of various wavelengths incident at normal and oblique angles. (b,d) Simulated focal spots produced by the singlet (b) and triplet (d) when focusing a broadband source in the wavelength range of 1.30 to 1.60 μm. Scale bar: 10 μm.

Figure 1(a, c) compares the focusing of a bundle of rays of light by a metalens singlet designed for a single wavelength to focus normally incident light and a triplet correcting both chromatic and monochromatic aberrations. There are significant aberrations for the singlet at oblique incident angles. These aberrations are suppressed for a properly designed triplet system. Figures 1(b, d) further compare a singlet and an aberration corrected triplet metalens with the same numerical aperture (NA) by showing simulated polychromatic focal plane intensity distributions at various angles of incidence. We can clearly observe the aberrations in the focal spots produced by the singlet and much reduced aberrations in those formed by the triplet. We design our aberration-corrected metalens triplet using conventional ray-tracing techniques (see, e.g., Ref. [52]) by minimizing the root mean square (RMS) focal spot sizes for a range of incident angles simultaneously through an appropriate choice of phase profiles for all three constituent metasurfaces. This approach simultaneously minimizes monochromatic aberrations including comatic, spherical, and field curvature. In the optimization process, the phase profile for each metasurface is parametrized as an even-ordered polynomial,

$$\boldsymbol{\Phi}^{(m)}(\boldsymbol{r}) = \sum_{n=1}^{5} \boldsymbol{a}_{\boldsymbol{n}}^{(m)} \left(\frac{\boldsymbol{r}}{\boldsymbol{R}^{(m)}}\right)^{2n} \qquad (1)$$

where r is the radial coordinate and $R^{(m)}$ is the radius of the "m^{th}" metasurface element. This optimization is done for a single wavelength, λ_{center}, that lies at the center of the desired operation wavelength range. The optimized phase profile at any another wavelength, λ, within the spectral range can be derived by scaling the phase profile at λ_{center} by a factor of λ/λ_{center}. For achromatic operation, each metasurface must provide simultaneously these desired phase and phase-dispersion profiles. To that end, our approach, outlined previously [39], employs high-index dielectric nano-pillars with engineered cross-sectional shapes to provide wavelength-dependent phase responses with subwavelength spatial resolution. By restricting the cross-sections to be four-fold symmetric and by only using five archetypes of cross-sectional shapes, we generate a library of polarization insensitive meta-atoms providing the maximum theoretically allowed coverage of phase dispersion determined by the wavelength-dependent modal overlap between light and the meta-atoms. Some example meta-atoms are shown in Fig. 2(c).

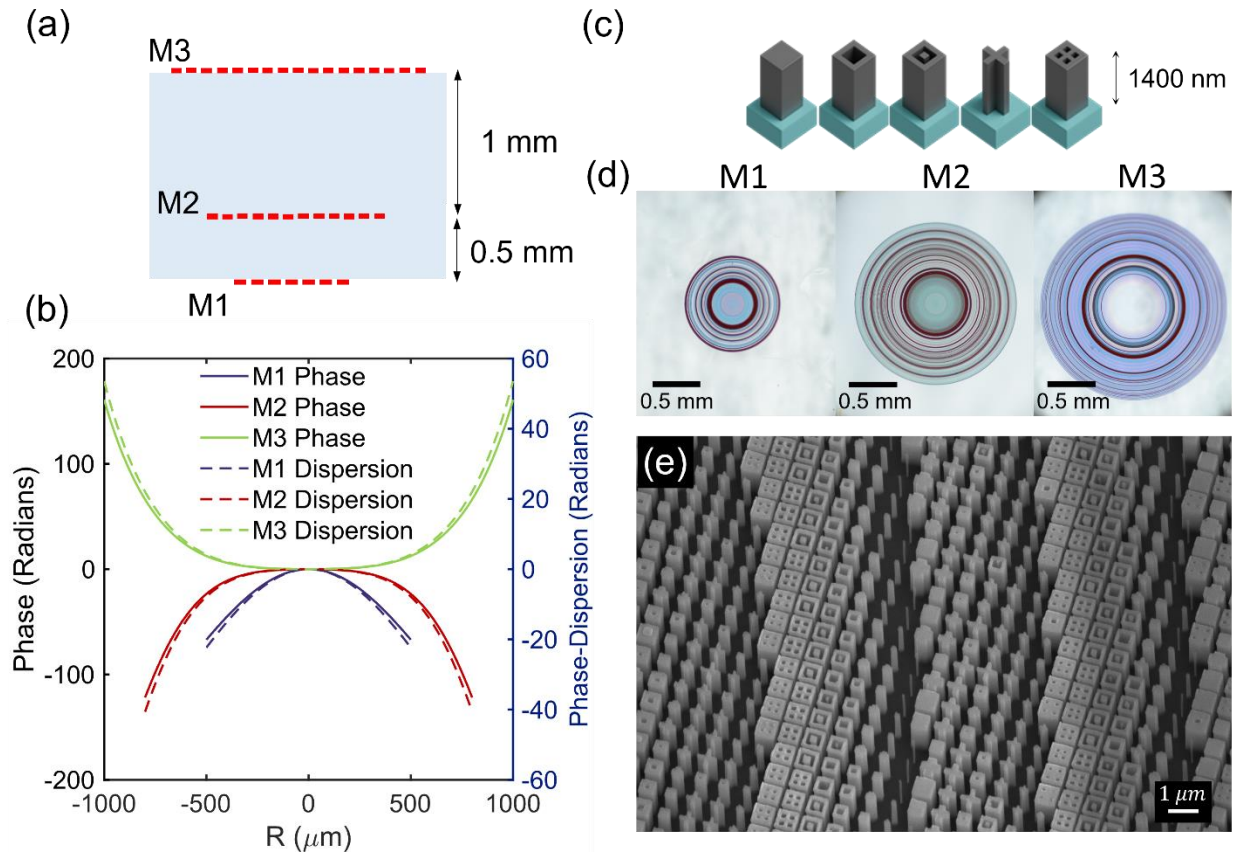

Fig. 2. Metalens triplet. (a) Schematic of the triplet. Light is incident on metasurface element M1 and light waves emanating from M3 form the focal spot. (b) Required phase profile at the central wavelength and dispersion profile for the three metasurface elements. Phase dispersion is defined here as the phase difference between wavelengths of 1.30 μm and 1.60 μm. (c) Amorphous silicon meta-atom archetypes utilized in realizing the metasurfaces. (d) Optical images of fabricated elements. (e) Scanning electron microscope image of a section of M1.

As derived in our previous work [39], the coverage of the phase-dispersion space by a meta-atom library sets a trade-off space between the achievable radius and NA of an achromatic metalens with a given operation bandwidth (see also Ref. [53]). This trade-off applies to each of the three metasurfaces comprising the triplet. Hence, the aperture size and the NA of the triplet system with chromatic aberration correction will be limited. Our choice of implementing a triplet instead of a doublet is motivated by the consideration that an additional element allows us to share the task of providing the range of phase dispersion needed for achieving a fixed focusing power among more metasurfaces. With these considerations, we have designed a metalens triplet composed of metasurfaces with radii of 0.4, 0.8, and 1 mm and a focal length of 5 mm defined from the last metasurface, resulting in an effective NA of 0.06. The triplet is optimized to correct chromatic

aberration for the wavelength range of 1,300 – 1,600 nm in the near-infrared with a FOV of 50°. A schematic of the optimized triplet system is shown in Fig. 2(a). The phase and phase dispersion profiles resulting from the ray-tracing optimization of the three metasurfaces are plotted in Fig. 2(b) (see Supplementary Material, Table S1 for the coefficients defining the profiles). We then choose the meta-atoms pointwise across the device according to an average spectral phase minimization error method [32], aiming to best satisfy these phase and phase dispersion values at each position of the metasurfaces. The archetypes of meta-atoms used to populate these metasurfaces are shown in Fig. 2(c). They are 1,400-nm tall amorphous silicon (a-Si) pillars arranged in a square lattice with a lattice constant of 700 nm [39].

The metasurfaces are fabricated by defining hard masks on a-Si-on-quartz chips using electron beam lithography, followed by reactive ion etching (see Supplement Material, Methods section for details). Alignment marks are defined on each of the chips for the purpose of stacking, which is done by mounting each individual metasurface on a separate 3D stage and bringing them together. The optical images of the fabricated metasurfaces and a scanning electron micrograph of one section of a metasurface are shown in Figs. 2d and 2e, respectively.

We characterize (see Supplement Material, Methods section for details) the performance of the triplets by measuring the 3D optical intensity distributions produced by the triplet system while illuminating it with a collimated beam with tunable wavelengths and incident angles using the setup shown in Fig. S4. The axial (X-Z cross-section) intensity distributions at normal incidence over a wavelength range of 1,200 – 1,600 nm are shown in Fig. S1(a), demonstrating that chromatic aberration across the wavelength range has been significantly suppressed. In Fig. 3(a), we show the measured intensity distributions as a function of wavelength and angle of incidence at the designed focal plane (see Supplement Material, Fig. S2 for simulation results), demonstrating close to diffraction-limited focusing up to an incident angle of 25 degrees across the designed wavelength range. A comparison of line cuts through these focal spots and the diffraction-limited spots is shown in Fig. S1(b). The slight asymmetric nature of some of the focal spots can be attributed to misalignment of the metasurfaces, limited by human error and resolution in the manual alignment process (in our demonstrations, the metasurfaces were fabricated independently, mounted on translation stages, and brought into position by hand). The degradation of focal spots at 25 degrees at short wavelengths can be attributed to the excitation of multiple waveguide modes in meta-atoms at that angle of incidence. We compute the polychromatic modulation transfer function (MTF) (see

Fig. S3 for monochromatic MTFs) from these measured focal plane intensities and plot them in Fig. 3(b). For each incident angle, the normalized focal spot intensity distributions at different wavelengths are summed and polychromatic MTF is calculated by taking the Fourier transform of the sum. The deviation away from the ideal diffraction limit of the MTF can be attributed to the reasons described above (i.e., misalignment between metasurfaces, excitation of higher-order modes in meta-atoms) and also to the large pixel size (20 μm) of our near-infrared camera.

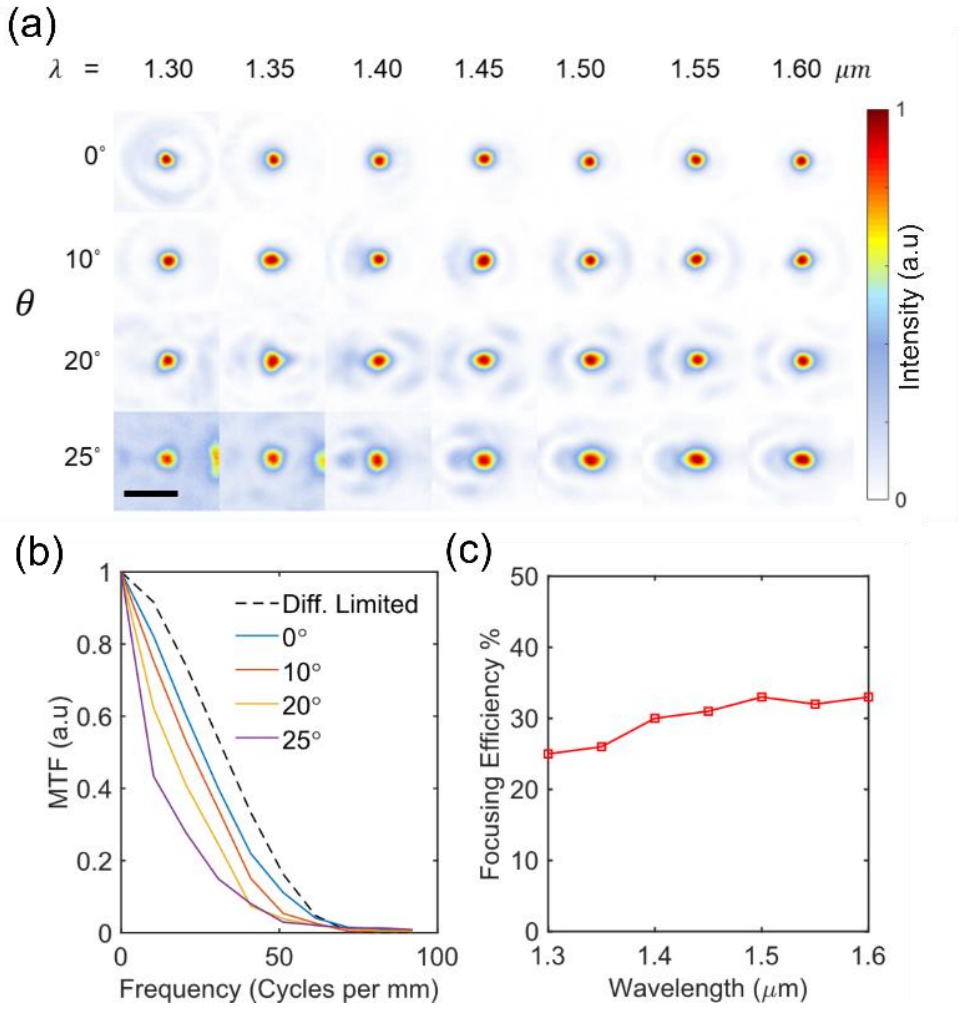

Fig. 3. (a) Measured normalized focal plane intensity distributions at various wavelengths and angles of incidence. (b) Polychromatic modulation transfer functions (MTFs) for each incident angle in (a). (c) Measured focusing efficiency at normal incidence as a function of wavelength.

We measure the focusing efficiency, which is defined as the ratio of power in the focal spots over the power incident on the input aperture of the triplet system, and show the result in Fig. 3(c). Focusing efficiencies of ~30% are observed for normal incidence over the entire wavelength range

of operation. The sources of reduced efficiency in the triplet are fabrication errors, nearest neighbor coupling between meta-atoms producing anomalous phase responses [54], and imperfect coverage of the phase-dispersion space by our meta-atom library [39], producing a mismatch between the required and the provided response at certain positions. Additionally, lack of anti-reflection coating on the surfaces produces unwanted back reflection and further contributes to reduced efficiency of the triplet.

Using the setup shown in Figs. S5 and S6, we conduct broadband, widefield imaging using the metalens triplet. A US Air Force resolution target transparency is illuminated with a narrowband diode laser (λ=1,550 nm) and imaged using the triplet. A 10× objective and a tube lens are used to magnify and relay the image formed by the triplet to the camera sensor. To avoid speckles, a rotating diffuser plate is used before the transparency. The image captured by the sensor is shown in Fig. 4(a). As a comparison, a halogen lamp producing broadband near-infrared radiation (see Supplement Material, Fig. S7 for its spectrum) is used to illuminate the same target and the image formed is shown in Fig. 4(b). We do not observe a significant presence of blur in the image that could be produced by defocus of different parts of the spectrum, demonstrating the achromatic focusing capability of the triplet. We also image a printout of the Columbia Engineering logo that is 10 cm wide and placed 15 cm away from the triplet under the broadband near-infrared illumination generated by the halogen lamp. The image shown in Fig. 4(c) illustrates broadband monochromatic aberration correction within a FOV of ±20°. Figure 4d shows the image of a similarly sized resolution target placed at the same distance from the triplet as in Fig. 4(c). Using the same setup, we also record a video in the near-infrared using the triplet, which shows the viability of our design for practical applications (see Supplement Material, Movie 1).

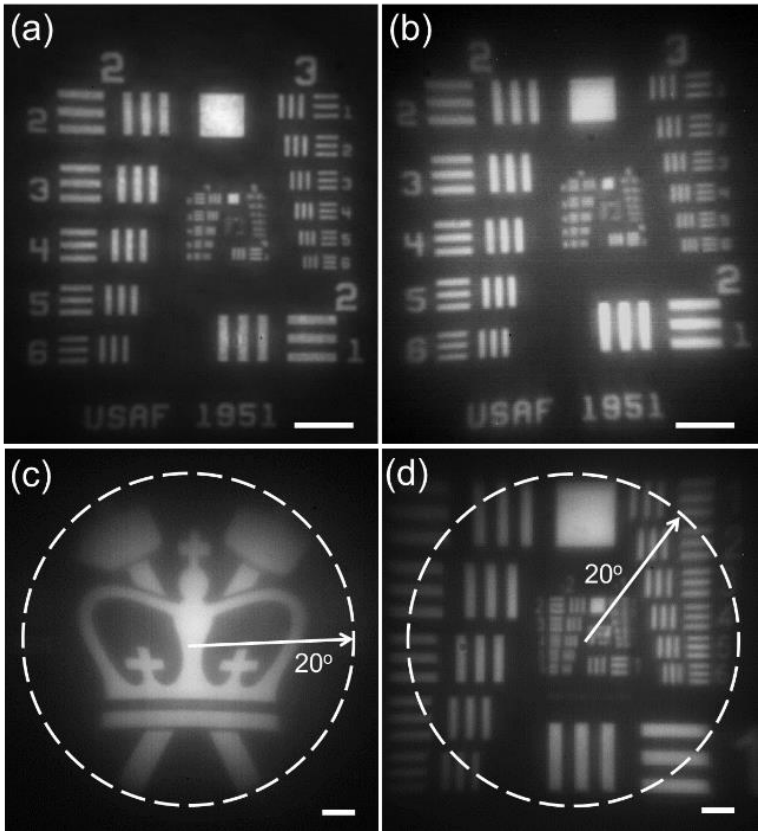

Fig. 4. Imaging using the metasurface triplet. (a,b) Images, captured using the triplet, of the US Airforce resolution target transparency illuminated by a narrow linewidth telecom diode laser (a) and a broadband near-infrared source (b). Scale bar: 1 mm. (c,d) Widefield images of Columbia Engineering logo and US Airforce target printouts illuminated by a broadband near-infrared source captured by the triplet. Dashed line represents ±20° FOV. Scale bar: 10 mm.

Metasurface-based optical elements will become increasingly attractive for use in compact imaging systems if their overall performance can reach similar levels as their counterparts based on refractive elements. Our work outlines a methodology to realize an optical-aberration-correction scheme in multi-element metasurface systems in order to achieve that goal. This design scheme can also be extended for non-imaging optical systems based on multi-element metasurfaces such as spectrometers and holograms. We have demonstrated that such a system can be optimized by using ray-tracing approaches already used by professionals in this field and therefore expect to see increasing adoption of metasurfaces elements in hybrid refractive-diffractive systems for various applications.

Our design can be scaled to other wavelength ranges by appropriately choosing the materials platform. In particular, high-index transparent dielectric materials are highly suitable for producing meta-atoms with diverse phase and dispersion responses via structural engineering.

Highly efficient dielectric metasurfaces in the visible have been reported using titanium dioxide [24] on quartz substrates and gallium nitride [38] on sapphire substrates. We note that our approach employs the "local phase approximation", the conventional metasurface design paradigm [16] that treats each meta-atom as producing an idealized spherical Huygens' wavelet, independent of nearest neighbors and incident angle. In our devices, given the height, refractive index, and period of the meta-atoms relative to the operating wavelength, resonant and nonlocal behaviors [55],[56] likely reduce the efficiency of operation, especially at the lower wavelengths. Future work may aim to go beyond this approximation to improve the efficiency [54]. Additionally, while the optimization procedure minimizes mismatch between required phase and actual phase, residual mismatch is present (see Fig. S8 and Table S2), leading to unwanted scattering. Finally, we note that the efficiency here is limited both by fundamental considerations [53], and by the limited average transmittance of the meta-atom library of 0.75 [39], which suggests an estimated upper bound in efficiency of $0.75^3=0.42$.

In conclusion, we have outlined a design paradigm to realize simultaneous correction of chromatic and monochromatic aberrations in multi-element metasurface systems. We experimentally demonstrated a metasurface triplet working in the near-infrared and showed polarization independent, near-diffraction limited, broadband imaging with a FOV spanning ± 25°. Metasurfaces can be mass manufactured on large wafers and stacked with high precision using conventional nanofabrication process lines. A significant advantage of metasurface-based optical systems is the possibility of direct integration of these elements on top of imaging sensors, which avoids the often-costly alignment process required when integrating refractive lens systems with imaging sensors in post-production. Leveraging such an integrated manufacturing process can reduce the cost and production time of high-performance optical systems particularly for compact optical systems for applications ranging from machine vision and metrology to virtual/augmented reality goggles and medical diagnostics.

Funding. This work was supported by the Defense Advanced Research Projects Agency (no. D15AP00111), the Air Force Office of Scientific Research (no. FA9550-14-1-0389 and no. FA9550-16-1-0322), and the National Science Foundation (no. ECCS-2004685 and QII-TAQS-1936359). A.C.O. acknowledges support from the NSF IGERT program (grant no. DGE-1069240). Research was carried out in part at the Center for Functional Nanomaterials, Brookhaven National Laboratory, which is supported by the US Department of Energy, Office of Basic Energy Sciences (contract no. DE-SC0012704), and in part at the Advanced Science Research Center (ASRC) NanoFabrication Facility at the Graduate Center of the City University of New York.

Supplemental document. See Supplement Material and Supplementary Movie 1 for supporting content.

Intellectual property. S.S., A.O., and N.Y. have a patent WO2018218063A1 entitled "Broadband achromatic flat optical components by dispersion-engineered dielectric metasurfaces" that is related to the technology reported in this Letter.

Conflicts of interest. The authors have no conflicts to disclose.

Data Availability Statement. The data supporting the findings are available in this article and its supplementary materials.

Acknowledgments. We thank M. Lipson, Predrag Milojkovic, Ramzi Zahreddine, and Rohith Chandrasekar for helpful discussions.

REFERENCES

[1] A. Arbabi, E. Arbabi, S. M. Kamali, Y. Horie, S. Han, and A. Faraon, Nat. Commun. **7**, 13682 (2016).
[2] B. Groever, W. T. Chen, and F. Capasso, Nano Lett. **17**, 4902 (2017).
[3] Y.-C. Chang, M.C. Shin, C.T. Phare, S.A. Miller, E. Shim, and M. Lipson, Optics Express **29**, 954-964 (2021).
[4] R.J. Martin, E. Marinov, M.A.B. Youssef, et al. Nature Communications **13**, 5724 (2022).
[5] G.-Y. Lee, J.-Y. Hong, S. Hwang, S. Moon, H. Kang, S. Jeon, H. Kim, J.-H. Jeong, and B. Lee, Nature Communications **9**, 1 (2018).
[6] J.-H. Song, J. van de Groep, S.J. Kim, and M.L. Brongersma, Nat. Nanotechnol. **16**, 1224-1230 (2021).
[7] Z. Li, R. Pestourie, J. Park, Y.W. Huang, S.G. Johnson, and F. Capasso, Nat. Communs. **14**, 2409 (2022).
[8] S. Zhang, C.L. Wong, S. Zeng, R. Bi, K. Tai, K. Dholakia, and M. Olivo, Nanophotonics **10**, 259-293 (2021).
[9] J. M. Geary, Introduction to Lens Design: With Practical ZEMAX Examples (Willmann-Bell, 2002).
[10] A. V. Kildishev, A. Boltasseva, and V. M. Shalaev, Science **339**, 1232009 (2013).
[11] F. Aieta, P. Genevet, M. A. Kats, N. Yu, R. Blanchard, Z. Gaburro, and F. Capasso, Nano Lett. **12**, 4932 (2012).
[12] P. Genevet, F. Capasso, F. Aieta, M. Khorasaninejad, and R. Devlin, Optica **4**, 139 (2017).
[13] N. Yu, P. Genevet, M. A. Kats, F. Aieta, J.-P. Tetienne, F. Capasso, and Z. Gaburro, Science **334**, 333 (2011).
[14] A. Pors, M. G. Nielsen, R. L. Eriksen, and S. I. Bozhevolnyi, Nano Lett. **13**, 829 (2013).
[15] D. Lin, P. Fan, E. Hasman, and M. L. Brongersma, Science **345**, 298 (2014).
[16] N. Yu and F. Capasso, Nat. Mater. **13**, 139 (2014).
[17] Y.-W. Huang, W. T. Chen, W.-Y. Tsai, P. C. Wu, C.-M. Wang, G. Sun, and D. P. Tsai, Nano Lett. **15**, 3122 (2015).
[18] G. Zheng, H. Mühlenbernd, M. Kenney, G. Li, T. Zentgraf, and S. Zhang, Nat. Nanotechnol. **10**, 308 (2015).
[19] R. C. Devlin, A. Ambrosio, N. A. Rubin, J. P. B. Mueller, and F. Capasso, Science **358**, 896 (2017).
[20] L. Wang, S. Kruk, H. Tang, T. Li, I. Kravchenko, D. N. Neshev, and Y. S. Kivshar, Optica **3**, 1504 (2016).

[21] X. Ni, A. V. Kildishev, and V. M. Shalaev, Nat. Commun. **4**, 2807 (2013).
[22] B. Wang, F. Dong, D. Yang, Z. Song, L. Xu, W. Chu, Q. Gong, and Y. Li, Optica **4**, 1368 (2017).
[23] A. Arbabi, Y. Horie, M. Bagheri, and A. Faraon, Nat. Nanotechnol. **10**, 937 (2015).
[24] M. Khorasaninejad, W. T. Chen, R. C. Devlin, J. Oh, A. Y. Zhu, and F. Capasso, Science **352**, 1190 (2016).
[25] S. M. Kamali, E. Arbabi, A. Arbabi, and A. Faraon, Nanophotonics **7**, 1041 (2018).
[26] A. Arbabi, Y. Horie, A. J. Ball, M. Bagheri, and A. Faraon, Nat. Commun. **6**, 7069 (2015).
[27] P. Lalanne, S. Astilean, P. Chavel, E. Cambril, and H. Launois, Opt. Lett. **23**, 1081 (1998).
[28] F. Yesilkoy, E. R. Arvelo, Y. Jahani, M. Liu, A. Tittl, V. Cevher, Y. Kivshar, and H. Altug, Nat. Photonics **13**, 390 (2019).
[29] N. A. Rubin, G. D'Aversa, P. Chevalier, Z. Shi, W. T. Chen, and F. Capasso, Science **365**, eaax1839 (2019).
[30] A. Arbabi, E. Arbabi, Y. Horie, S. M. Kamali, and A. Faraon, Nat. Photonics **11**, 415 (2017).
[31] A. Y. Zhu, W. T. Chen, J. Sisler, K. M. A. Yousef, E. Lee, Y.-W. Huang, C.-W. Qiu, and F. Capasso, Adv. Opt. Mater. **7**, 1801144 (2019).
[32] R. J. Lin, V.-C. Su, S. Wang, M. K. Chen, T. L. Chung, Y. H. Chen, H. Y. Kuo, J.-W. Chen, J. Chen, Y.-T. Huang, J.-H. Wang, C. H. Chu, P. C. Wu, T. Li, Z. Wang, S. Zhu, and D. P. Tsai, Nat. Nanotechnol. **14**, 227 (2019).
[33] P. Hartmann, Optical Glass (SPIE Press, Bellingham, Washington, USA, 2014).
[34] T. Stone and N. George, Appl. Opt. **27**, 2960 (1988).
[35] W. T. Chen, A. Y. Zhu, J. Sisler, Y.-W. Huang, K. M. A. Yousef, E. Lee, C.-W. Qiu, and F. Capasso, Nano Lett. **18**, 7801 (2018).
[36] E. Arbabi, A. Arbabi, S. M. Kamali, Y. Horie, and A. Faraon, Optica **4**, 625 (2017).
[37] W. T. Chen, A. Y. Zhu, V. Sanjeev, M. Khorasaninejad, Z. Shi, E. Lee, and F. Capasso, Nat. Nanotechnol. **13**, 220 (2018).
[38] S. Wang, P. C. Wu, V.-C. Su, Y.-C. Lai, M.-K. Chen, H. Y. Kuo, B. H. Chen, Y. H. Chen, T.-T. Huang, J.-H. Wang, R.-M. Lin, C.-H. Kuan, T. Li, Z. Wang, S. Zhu, and D. P. Tsai, Nat. Nanotechnol. **13**, 227 (2018).
[39] S. Shrestha, A. C. Overvig, M. Lu, A. Stein, and N. Yu, Light Sci. Appl. **7**, 1 (2018).
[40] E. Almeida, O. Avayu, T. Ellenbogen, and Y. Prior, Nat. Commun. **8**, 14992 (2017).
[41] E. Arbabi, A. Arbabi, S. M. Kamali, Y. Horie, M. Faraji-Dana, and A. Faraon, Nat. Commun. **9**, 1 (2018).
[42] Y. Zhou, I. I. Kravchenko, H. Wang, J. R. Nolen, G. Gu, and J. Valentine, Nano Lett. **18**, 7529 (2018).
[43] F. Aieta, M. A. Kats, P. Genevet, and F. Capasso, Science **347**, 1342 (2015).
[44] E. Arbabi, A. Arbabi, S. M. Kamali, Y. Horie, and A. Faraon, Optica **3**, 628 (2016).
[45] D. Sell, J. Yang, S. Doshay, and J. A. Fan, Adv. Opt. Mater. **5**, 1700645 (2017).
[46] Z. Shi, M. Khorasaninejad, Y.-W. Huang, C. Roques-Carmes, A. Y. Zhu, W. T. Chen, V. Sanjeev, Z.-W. Ding, M. Tamagnone, K. Chaudhary, R. C. Devlin, C.-W. Qiu, and F. Capasso, Nano Lett. **18**, 2420 (2018).
[47] X. Li, L. Chen, Y. Li, X. Zhang, M. Pu, Z. Zhao, X. Ma, Y. Wang, M. Hong, and X. Luo, Sci. Adv. **2**, e1601102 (2016).
[48] S. M. Kamali, E. Arbabi, A. Arbabi, Y. Horie, M. Faraji-Dana, and A. Faraon, Phys. Rev. X **7**, 041056 (2017).
[49] C. Kim, S.-J. Kim, and B. Lee, Optics Express **28**, 18059 (2020).

[50] Z. Huang, M. Qin, X. Guo, C. Yang, and S. Li, Optics Express **29**, 13542 (2021).
[51] S. Luo, F. Zhang, X. Lu, et al. J. Phys. D: Appl. Phys. **55**, 235106 (2022).
[52] C. P. Castañeda-Almanza and Ivan Moreno, "Ray tracing in metasurfaces", Optics Continuum **1**, 858-964 (2022).
[53] F. Presutti and F. Monticone, Optica **7**, 624-621 (2020).
[54] L. Hsu, M. Dupré, A. Ndao, et al. Optics Express **25**, 24974 (2017).
[55] A. Overvig and A. Alu, Laser & Photonics Reviews **16**, 2100633 (2022).
[56] K. Shastri and F. Monticone, Nat. Photonics **17**, 36-47 (2023).

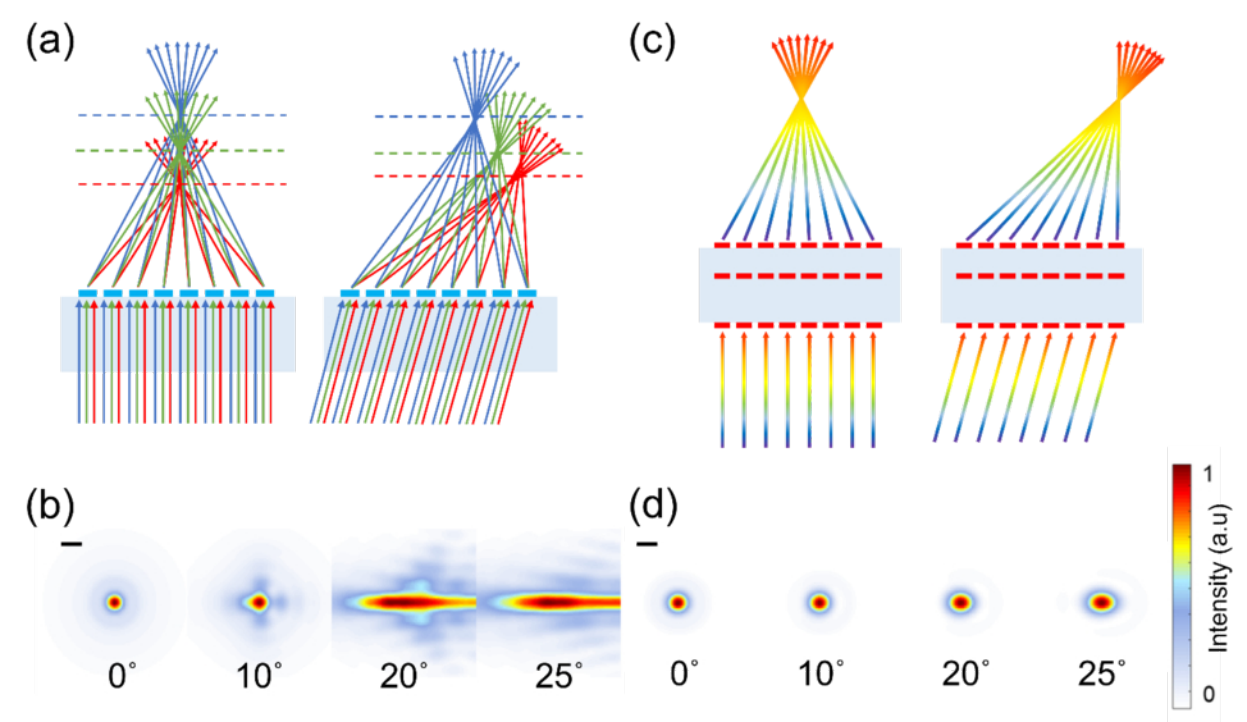
(a)
(c)
(b)
(d)
0°
10°
20°
25°
0°
10°
20°
25°
1
Intensity (a.u)
0

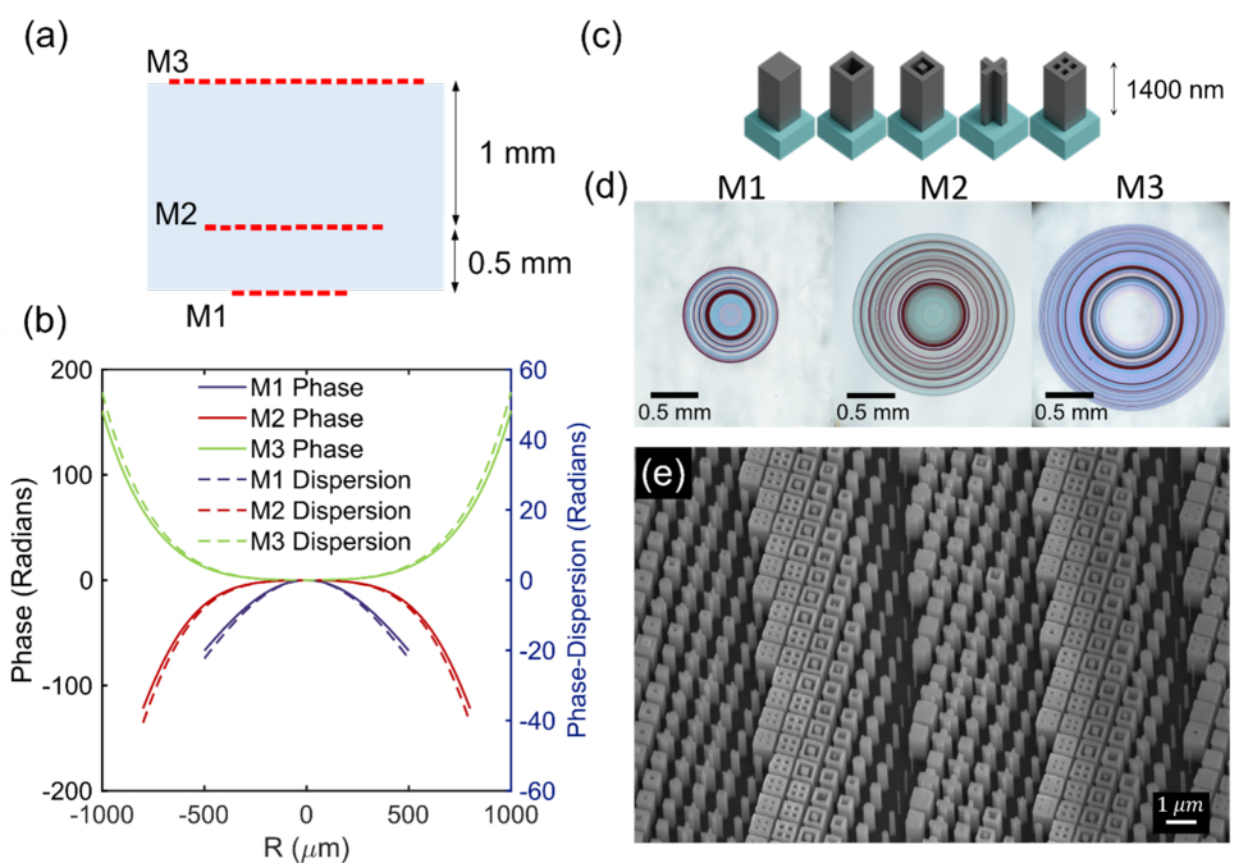
(a)
M3
M2
M1
1 mm
0.5 mm
(b)
M1 Phase
M2 Phase
M3 Phase
M1 Dispersion
M2 Dispersion
M3 Dispersion
Phase (Radians)
Phase-Dispersion (Radians)
R (μm)
200
100
0
-100
-200
60
40
20
0
-20
-40
-60
-1000
-500
0
500
1000
(c)
1400 nm
(d)
M1
M2
M3
0.5 mm
0.5 mm
0.5 mm
(e)
1 μm

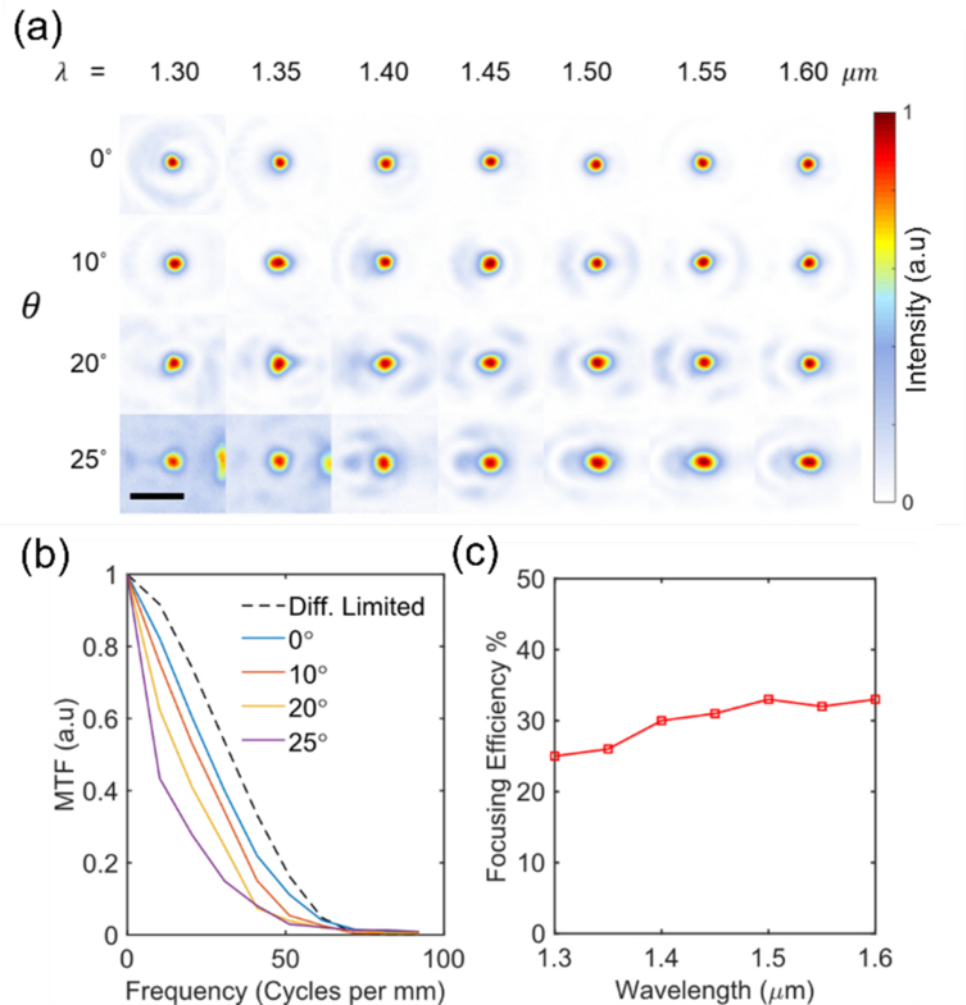
(a)
λ = 1.30 1.35 1.40 1.45 1.50 1.55 1.60 μm
θ
0°
10°
20°
25°
1
0
Intensity (a.u)
(b)
Diff. Limited
0°
10°
20°
25°
MTF (a.u)
Frequency (Cycles per mm)
(c)
Focusing Efficiency %
Wavelength (μm)

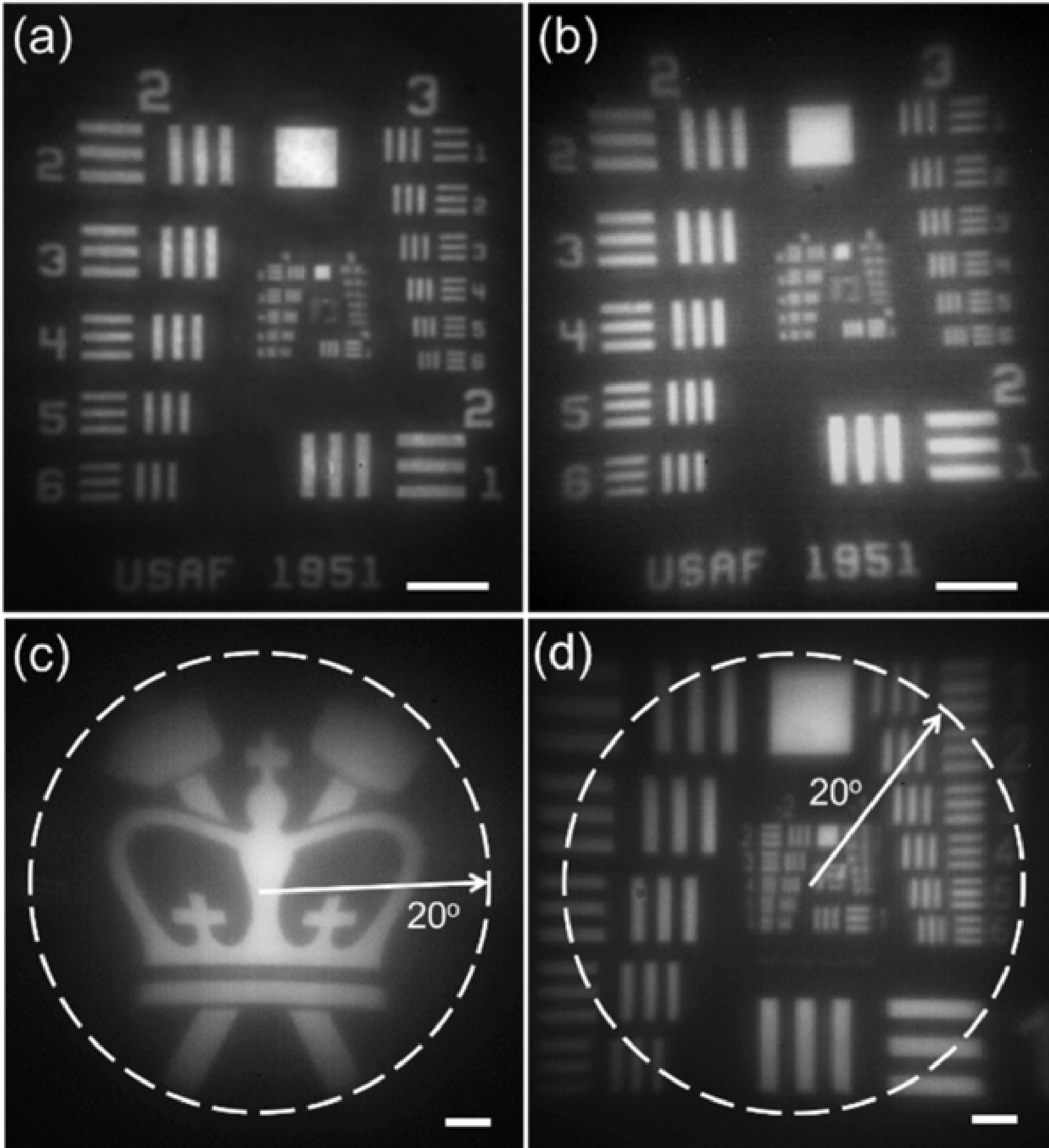
(a)
USAF 1951
(b)
USAF 1951
(c)
20°
(d)
20°